Project 1:

Lander Technical Report

Design and Report Credits to:

Sheila Zomoroddian

Gillian McCaw

Christian Parra

Brenden Vis

Introduction

Background and Objective

With the advent of traveling to Mars, there comes a need to efficiently land on the Red Planet's surface. As outlined by Dr. Hemmati, the objective of this project is to design a fuelless, stackable lander that is able to be deployed on a planetary surface in order to collect data at multiple locations simultaneously. There are many benefits to using fuelless systems. First, they allow for more flexibility when designing the overall vehicle. The reason for this is that without the need for fuel, one can have more options in terms of payload, or perhaps one would opt for a smaller, lighter vehicle. Second, along the same lines, is cost reduction. If all that is being left out is the fuel that would have been needed to land, the cost of purchasing that fuel would be available for other parts of the mission. Third, it reduces the complexity of the system in terms of points of failure, which is always a net positive when working in the conditions of space or another planet. In this project autorotation is used to create landers that do not need fuel. Autorotation relies on the movement of air around the blades to cause the blade to rotate and have a controlled descent without the use of a control system. When it comes to this design specifically, there are benefits to mission efficiency. Overall, the geometry of the lander craft offers advantages in terms of space efficiency when storing and transporting it to Mars. This advantage is afforded by the thin, disk-like shape of the lander, granting it a stacking ability for easy and efficient storage within a spacecraft. This allows for many landers to be carried by one launch vehicle and subsequently deployed all over the planet for mass coverage serving whatever purpose necessary. All of these benefits thoroughly justify the need for a fuelless planetary lander system.

How is this a Complex Engineering Problem?

This project is a complex engineering problem according to the standards put forth by the ABET Definition of Complex Engineering. It involves wide-ranging or conflicting technical issues, with the conflicting issues being that of strength versus weight. In order to create a stackable geometry it was required to create a relatively flat design which required careful mass considerations. The blades had to be long in order to generate enough lift however if the design was too heavy it would be unable to stay afloat. This is an age-old conflict when it comes to aerospace engineering problems and like any other, this problem prioritizes a balance between the two qualities. The added aspect of being fuelless was a unique problem with no obvious solution. It required thinking outside of the box, looking to nature to find a way to control the descent of the lander and incite rotation without typical electrical controls or engine. Many problems beyond typical aerodynamics had to be addressed including stackable geometry, fuelless system, recording data, and accounting for atmosphere's other Earth. Incorporated into this project were many disciples of engineering. Simulating data and design required a complex understanding of aerodynamics to optimize lift and achieve autorotation. Structural considerations had to be made to ensure the mass of the craft did autorotate. The sensor inside the camera required programming, as well as simulations. The design and testing of planetary landers requires an in-depth understanding of aerospace engineering and the atypical nature of the design makes the project a complex engineering problem.

Configuration Data

Geometry

Fuselage Height [m]	Fuselage Radius [m]	Overall Radius [m]	Wing Radius [m]
.075	.0425	.4743	.4318

Table 1: Overall Dimensions.

Blade Span R [m]	Blade Area $[m^2]$	Twist Angle (max)	Twist Angle (min)	Number of Blades
0.4318	0.0496773	30° at R = 0m	0° at R = 0.4318m	4

Table 2: Blade Properties.

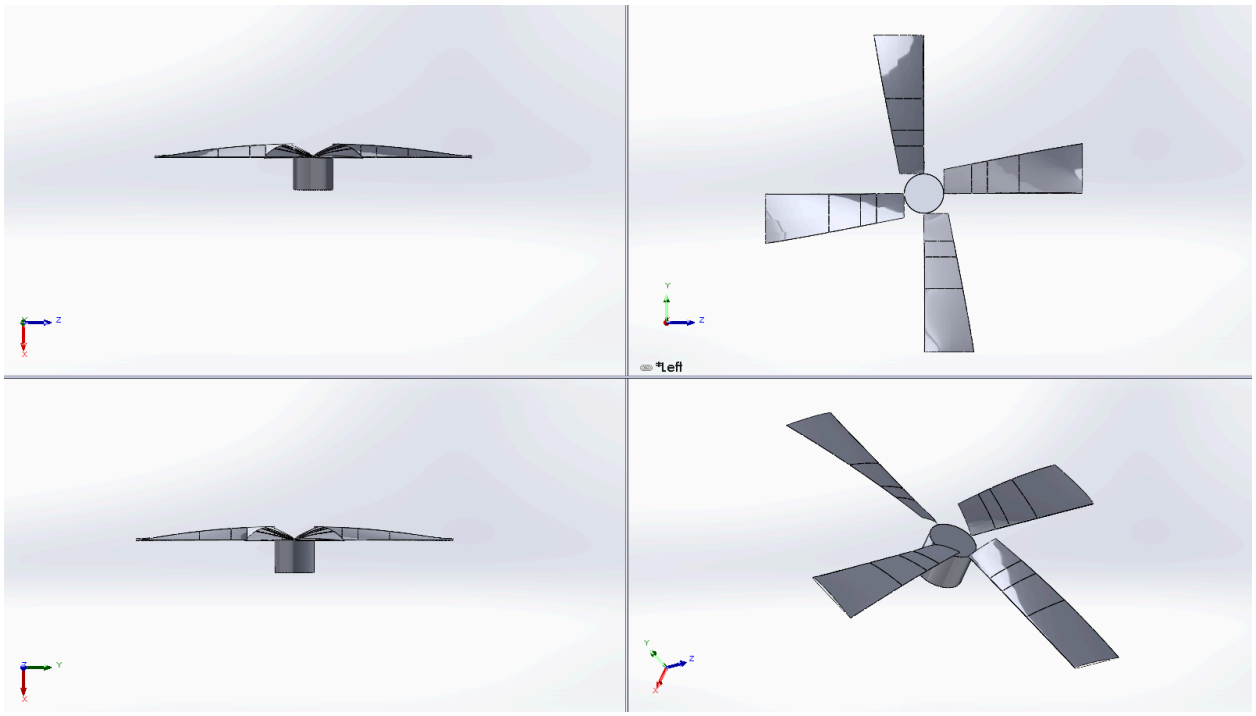

Figure 1: 4-view drawing.

Figure 2: Photo of Rotorcraft as Built.

Mass Properties

Each of the components of the rotorcraft were measured individually and then assembled. The results of these measurements are shown in **Table 3** below.

Component	Wing	Optical Sys.	Body	IMU Housing	Whole
Mass [g]	32.8	26.8	8.6	14.4	181

Table 3: Mass Breakdown of Major Components.

The mass properties of the rotor vehicle was calculated using the 3D model that was developed using OpenVSP. A volume based method to calculate mass properties was used where the density of each component was inputted and the program calculated each of the moments of inertia with the origin at the center of rotation of the rotor blade. The density used for the blades was higher than the density of raw foam due to additional materials on the blades including epoxy, paper, and duct tape. The density of the center mass was determined based on the weight of the whole body assembly. The analytical moments of inertia are seen in **Table 4** below.

I_{xx} [kg · m^2]	I_{yy} [kg · m^2]	I_{zz} [kg · m^2]	I_{xy} [kg · m^2]	I_{xz} [kg · m^2]	I_{yz} [kg · m^2]
0.0006257	0.0006257	0.0011529	0.0000005	0.0000000	0.0000000

Table 4: Moments of Inertia by Analytical Method.

The experimental moments of inertia were calculated using a swing balance where the rotorcraft was placed on the compound pendulum and then either swung or twisted. The time for the rotorcraft to return to the original position was recorded as the period T. Then the mass m, gravitational force g, and pendulum length L were then used to calculate the moments of inertia about the x and y axis. In addition to the previous variables, the distance between vertical ropes d and the length of the purely vertical part of the rope D were used to find the moment of inertia about the Z axis. **Equation 1** below was used to find the moment of inertia about the X and Y axis while **Equation 2** below was used to calculate the moment of inertia about the Z axis.

$$I = mL[\frac{T^2 g}{4\Pi^2} - L] \qquad \textbf{Equation 1}$$

$$I_{zz} = \frac{mgT^2 d^2}{16\Pi^2 D} \qquad \textbf{Equation 2}$$

The results of the experimental calculations of the rotor blade moment of inertia about the x, y, and z axis are recorded in **Table 5** below.

I_{xx} [kg · m^2]	I_{yy} [kg · m^2]	I_{zz} [kg · m^2]
.00074	.00074	.0014

Table 5: Moments of Inertia by Swing Balance Experiment.

Selected Airfoil

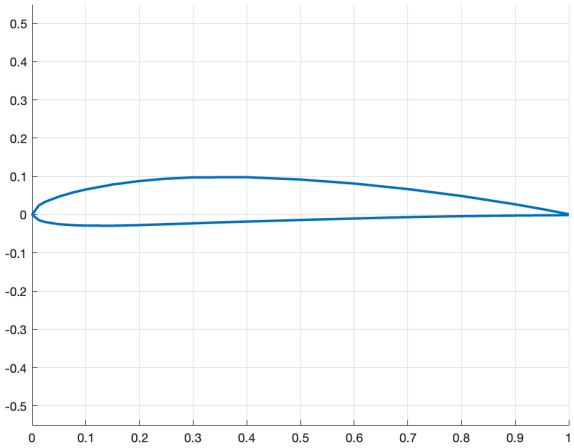

Figure 3: Side profile of NACA 4412 airfoil.

Coefficient of Lift and Drag

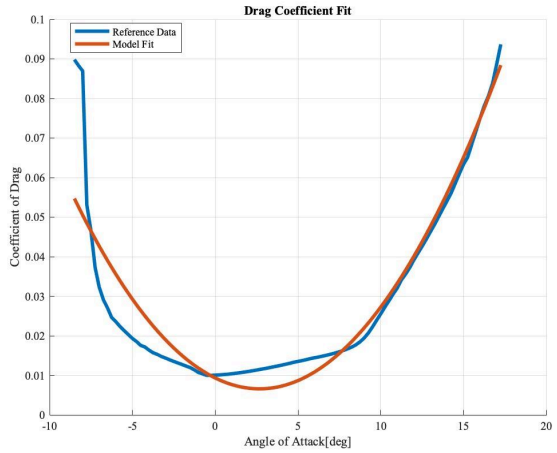

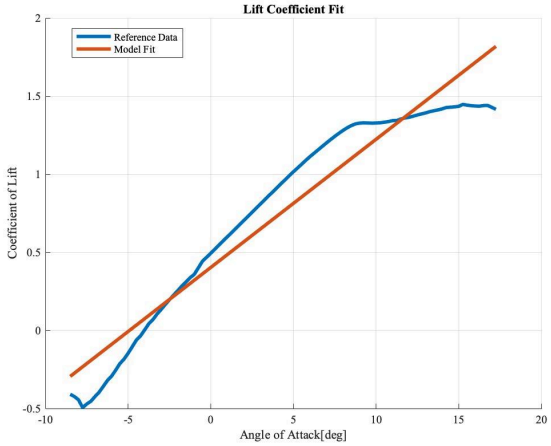

Figure 4a: Plot of Drag Coefficient vs Angle of Attack with Line of Best Fit.

Figure 4b: Plot of Lift Coefficient vs Angle of Attack with Line of Best Fit.

Equations used for Lines of Best Fit (α in radians):

$$C_D = 1.265\alpha^2 - 0.1181\alpha + 0.0093 \qquad C_L = 4.7\alpha + 0.4030$$

Figures 4a and **4b** were created using data for the NACA 4412 Airfoil at Reynold's number 200,000 from UIUC Airfoil Coordinates Database and creating a best fit polynomial of the data.

Aerodynamics

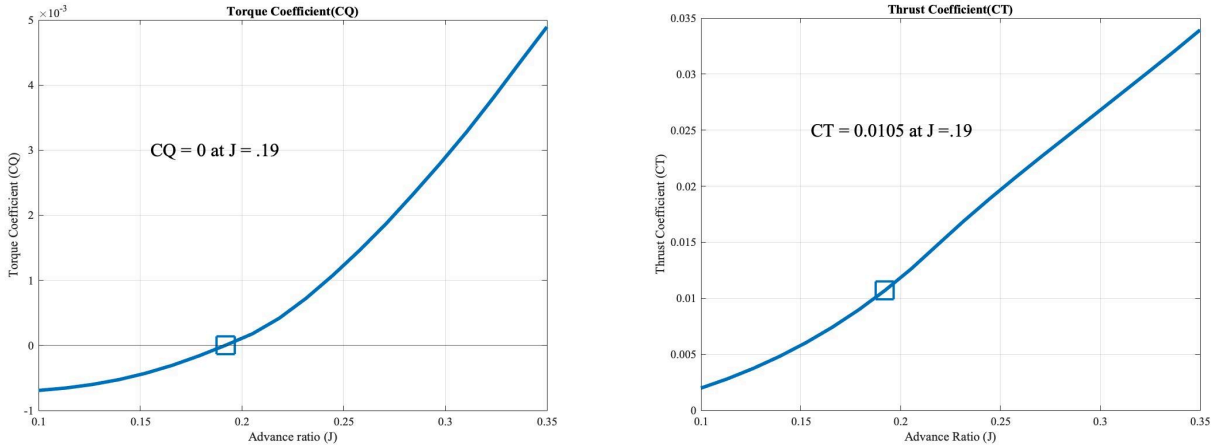

Figure 5a: Plot of Torque Coefficient vs. Advance Ratio.

Figure 5b: Plot of Thrust Coefficient vs. Advance Ratio.

Figure 5a reveals that the advance ratio at a torque coefficient of zero is 0.19, denoted by the blue square. This is the advance ratio used to make estimates for sink rate. The blue square in **Figure 5b** marks the thrust coefficient of the rotorcraft at the previously found advanced ratio. This thrust coefficient is used to estimate spin rate.

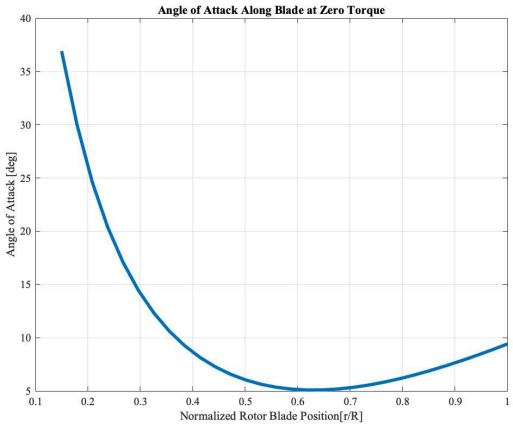

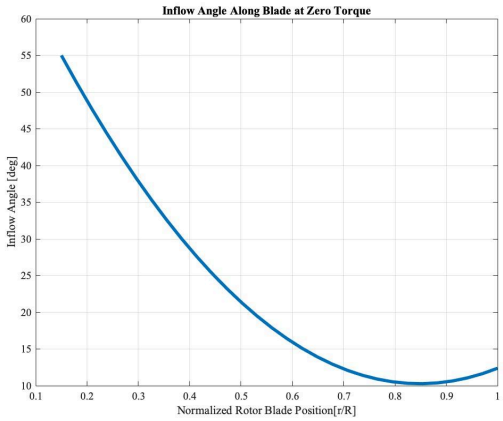

Figure 6a: Angle of attack vs. Normalized Rotor Blade Position.

Figure 6b: Inflow angle vs. Normalized Rotor Blade Position.

Figure 6a simulates the angle of attack which is the angle between the blade chord and air flow. Inflow angle is the angle of the blade with respect to the motion of the air and is depicted in **Figure 6b**. Airfoil sections below r/R = 0.15 are in stalled conditions. Both inflow angle and angle of attack steadily decrease before plateauing than slowly increasing toward a steady state. This motion indicates the rotorcraft accelerating before approaching a steady velocity as it descends.

$$\Omega = \frac{1}{R^2}\sqrt{\frac{mg}{C_T \rho \pi}} \qquad \textbf{Equation 3}$$

$$w = J\Omega R \qquad \textbf{Equation 4}$$

C_T	J	Spin Rate Ω [deg/s]	Sink Rate w [m/s]
0.0105	0.19	2080	2.98

Table 6: Predicted Values.

Equation 3 is used to calculate spin rate using the values of C_T and J indicated in **Table 6** as well as R from **Table 2**. For density and gravity sea level conditions were assumed therefore, $\rho = 1.225 \frac{kg}{m^3}$ and $g = 9.81 \frac{m}{s^2}$.

Flight Test

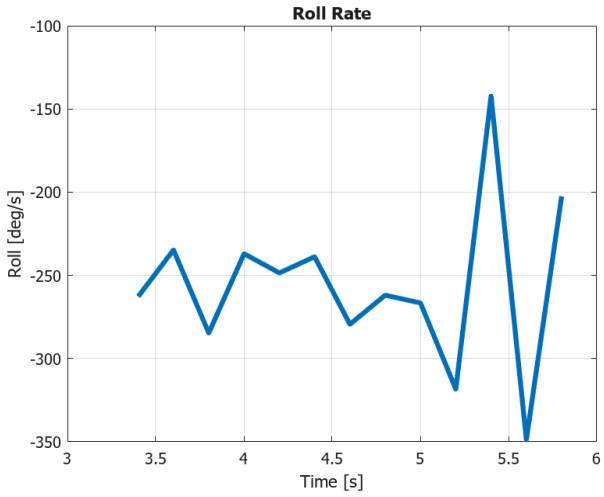

Figure 7: Roll Rate of the Rotorcraft vs. Time.

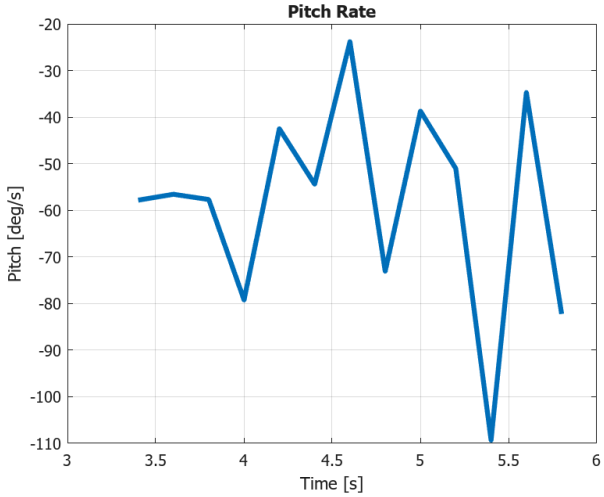

Figure 8: Pitch Rate of the Rotorcraft vs. Time.

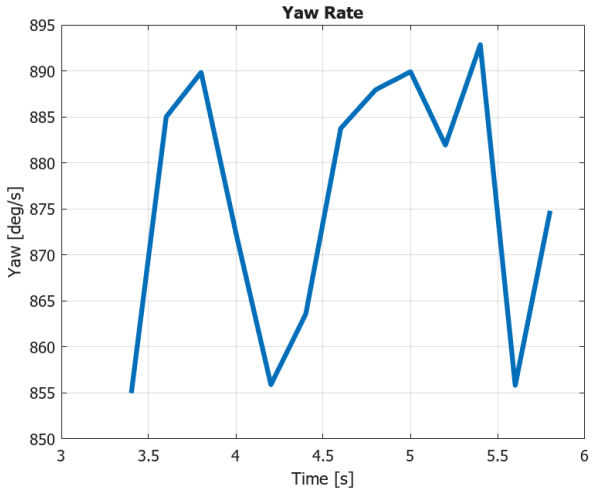

Figure 9: Yaw Rate of the Rotorcraft vs. Time.

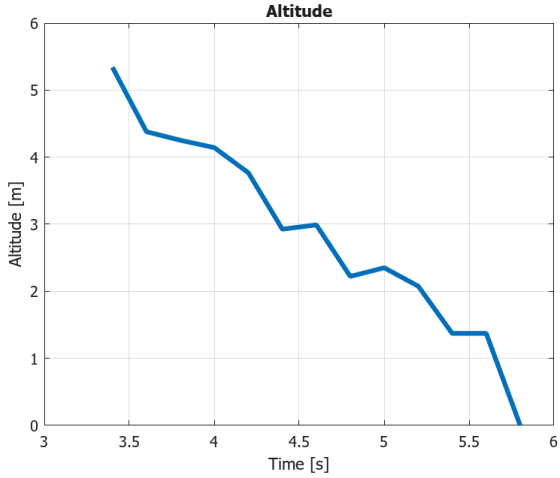

Figure 10: Altitude of the Rotorcraft vs. Time.

$$C_T = \frac{mg}{\rho\pi\Omega^2 R^4} \qquad \textbf{Equation 5}$$

$$J = \frac{w}{\Omega R} \qquad \textbf{Equation 6}$$

CT	J	Spin rate (Ω)	Sink Rate (w)
0.052	0.278	900.117 deg/s	1.88 m/s

Table 7: Experimental Values.

The experimental spin rate is taken as the average stable yaw rate. The experimental sink rate is taken as the average stable decent rate which was found using pressure data. Advance ratio and thrust coefficient were calculated using **Equation 5** and **Equation 6** using the spin and sink rate determined from experimental data. The experimental thrust coefficient, advance ratio, spin rate, and sink rate differ from the simulated data but are in the same order of magnitude. Experimental advance ratio and thrust coefficient are larger than simulated. This corresponds to sink and spin rate being slower than expected.

Conclusion

There are multiple reasons why the simulated data differs from real-world testing. The actual altitude for testing is slightly above sea level which could make the sea-level density assumption used in simulation inaccurate. Other conditions that potentially differed in real world testing causing discrepancies were pressure and humidity. These differences could contribute to a disparity between the simulated lift and the real-world lift. Wind and gusts present in real-world conditions were difficult to account for and could have led to differences in the results. Due to the flight test being performed outside, these effects were greater than were simulated and resulted in unpredictable roll and pitch results. During the testing process more surface area was added to the blade design to generate lift. The increased surface area was difficult to account for in the simulation which was designed for more standard blade shapes. The increased lift caused the craft to fall more slowly than what was originally simulated, which was ultimately the intention behind adding more surface area.

The purpose of this project was to create a lander that could be used on Mars. Mars, obviously as well as most notably, has a distinct lack of atmospheric density compared to Earth, leading to an overall loss of lift generated by the lander's airfoils and therefore a major loss in efficiency of the system. This condition may be in part offset by the fact that Mars has less mass and therefore lower gravity than Earth, thereby reducing the weight that must be lifted by the system. Another factor to consider is that Mars can often have massive and forceful dust storms that affect large parts of the surface for extended periods of time. These storms will undoubtedly make it difficult to land anything on the planet, let alone a lander that behaves at the whims of the local winds and atmosphere.

References

Selig, Michael S. (1996). UIUC airfoil data site. Urbana, Ill. :Department of Aeronautical and Astronautical Engineering University of Illinois at Urbana-Champaign.

Anderson, Mark. Lectures and Slides. MAE 155B UCSD, San Diego, 2024

Hemmati, H. Two-Dimensional Planetary Surface Landers. Jet Propulsion Laboratory, California Institute of Technology, Pasadena, 2014